

Neuron

Functional Convergence at the Retinogeniculate Synapse

Highlights

- Optogenetic analysis of convergence of RGCs in visual thalamus
- On average, ten RGCs functionally innervate mouse dLGN thalamocortical neurons
- 30% of functional RGC inputs dominate thalamic neuron activity; the remainder are weak
- Results reconcile connectomics with functional estimates of convergence

Authors

Elizabeth Y. Litvina, Chinfei Chen

Correspondence

chinfei.chen@childrens.harvard.edu

In Brief

Litvina and Chen address a controversial disconnect between functional and recent connectomic characterizations of retinogeniculate convergence. Few strong among many converging inputs dominate retinogeniculate transmission. Heterogeneity of synaptic strengths demonstrates potential complexity of visual thalamic function.



Functional Convergence at the Retinogeniculate Synapse

Elizabeth Y. Litvina^{1,2} and Chinfei Chen^{1,2,3,*}

¹Department of Neurology, F.M. Kirby Neurobiology Center, Children's Hospital, Boston, 300 Longwood Avenue, Boston, MA 02115, USA

²Program in Neuroscience, Harvard Medical School, 220 Longwood Avenue, Boston, MA 02115, USA

³Lead Contact

*Correspondence: chinfei.chen@childrens.harvard.edu

<https://doi.org/10.1016/j.neuron.2017.09.037>

SUMMARY

Precise connectivity between retinal ganglion cells (RGCs) and thalamocortical (TC) relay neurons is thought to be essential for the transmission of visual information. Consistent with this view, electrophysiological measurements have previously estimated that 1–3 RGCs converge onto a mouse geniculate TC neuron. Recent advances in connectomics and rabies tracing have yielded much higher estimates of retinogeniculate convergence, although not all identified contacts may be functional. Here we use optogenetics and a computational simulation to determine the number of functionally relevant retinogeniculate inputs onto TC neurons in mice. We find an average of ten RGCs converging onto a mature TC neuron, in contrast to >30 inputs before developmental refinement. However, only 30% of retinogeniculate inputs exceed the threshold for dominating postsynaptic activity. These results signify a greater role for the thalamus in visual processing and provide a functional perspective of anatomical connectivity data.

INTRODUCTION

Divergent and convergent synaptic circuits in the CNS form the substrate for complex computations underlying transmission of information between neurons. In the visual system, information is relayed from retina to visual cortex via the dorsal lateral geniculate nucleus (dLGN). The retinogeniculate synapse (RGS) in the dLGN is an experimental workhorse for developmental and systems neurobiology. Accumulating data from primates, cats, and mice have supported the view that thalamocortical relay (TC) neurons receive convergent inputs from one dominant retinal ganglion cell (RGC), with additional weaker RGC inputs evident in the cat (Cleland et al., 1971; Mastronarde, 1992; Usrey et al., 1999). *In vivo* recordings showed that one RGC input often dominates spiking of a TC neuron, and connected RGC-TC neuron pairs exhibit very similar center-surround receptive fields in cats and primates (Weyand, 2016). *In vitro* slice recordings also showed ~1–3 RGCs innervate a TC neuron in mice (Chen

and Regehr, 2000; Jaubert-Miazza et al., 2005). As each RGC encodes a unique feature in a point of visual space, this simple wiring diagram has suggested a limited role for the RGS in sensory integration.

Recent anatomical studies in mice using novel large-scale connectomics and retrograde viral tracing have challenged this view of retinogeniculate (RG) functional organization, showing that up to 91 RGCs may converge onto single TC neurons (Hammer et al., 2015; Morgan et al., 2016; Rompani et al., 2017). Such extensive RG convergence challenges existing models of RG function (Alonso et al., 2006; Martinez et al., 2014; Usrey and Alitto, 2015) and suggests significant thalamic processing and sensory integration of visual information. However, these studies were performed from postnatal day P21 to P42, when experience-dependent functional rewiring of the circuit and RGC axon retraction and pruning is still occurring (Hong et al., 2014). Therefore, many of the morphologically identified inputs may be remnants of refinement. Furthermore, these anatomical approaches did not distinguish between functionally strong, weak, and silent contacts. This distinction is important at the mouse RGS, because inputs exceeding 600 pA in amplitude are much more likely to drive TC neuron activity than weak inputs (Liu and Chen, 2008). Therefore, to understand the nature and degree of information processing in the dLGN, we used optogenetics to stimulate previously inaccessible retinal inputs in order to determine the overall number and strength of functionally relevant RG inputs. We find that, consistent with anatomical studies, more RGC inputs converge onto TC neurons than previously recognized in mice. However, only ~30% of these inputs are strong enough to dominate postsynaptic AP firing. Our results demonstrate a remarkable heterogeneity in strength of convergent RG inputs, ranging several orders of magnitude even in the adult, and support greater nuance in the role of the dLGN in vision.

RESULTS

Optogenetic Stimulation Recaptures Axons Severed in Slice

Estimates of RG convergence in rodents have relied on brain slice recordings and electrical stimulation (e-stim) of the optic tract (OT). This approach underestimates the number of afferent inputs, as axons can be severed in slice. To circumvent this limitation, we expressed channelrhodopsin (ChR2) in RGCs

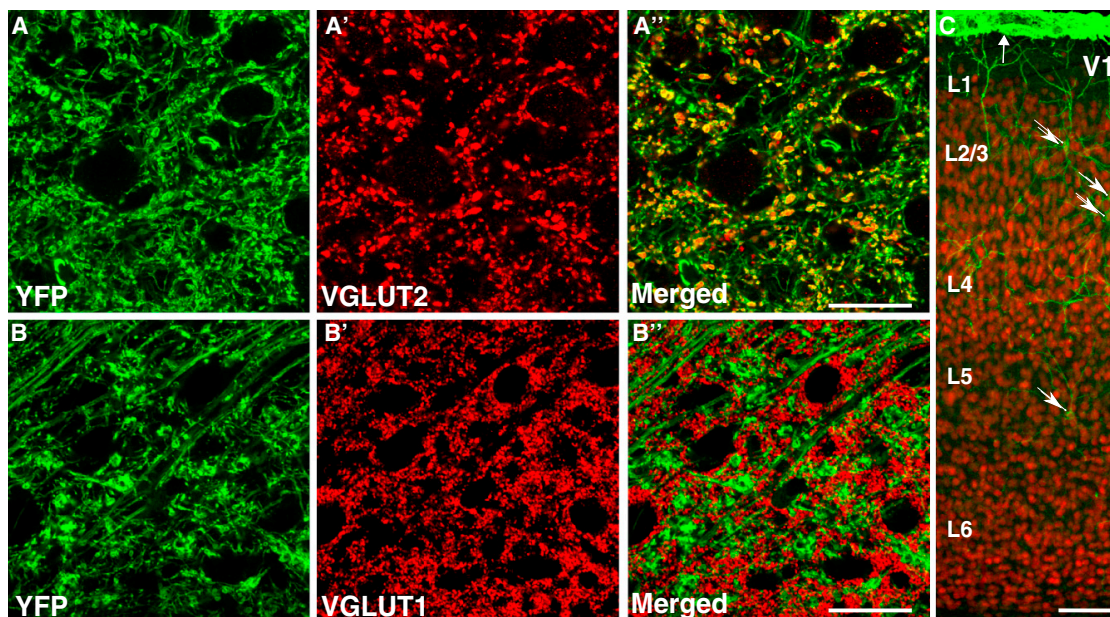


Figure 1. ChR2 Expression in dLGN Is Restricted to Retinal Inputs in *Chx10-Cre;ChR2* Mice

(A and B) High-mag view of dLGN. Co-immunostained for YFP+ (green, ChR2) and (A) VGLUT2 or (B) VGLUT1 (red). Most YFP+ boutons are also VGLUT2+, but VGLUT1-. Scale bar, 20 μ m.

(C) Sparse YFP labeling in the V1. Arrowheads, YFP+ neurons; arrow, non-neuronal YFP. Scale bar, 100 μ m.

See also Figure S1.

transgenically, enabling stimulation of presynaptic RGC terminals, including those from severed axons. *Chx10-Cre* mice, which express Cre recombinase as early as embryonic day 9 (E9) in retina (Rowan and Cepko, 2004), were crossed with Cre-dependent ChR2(H134R)-EYFP (Ai32; Madisen et al., 2012).

Postnatally, *Chx10-Cre;ChR2* mice express YFP in the retina, including RGC somas (Figure S1A) and axon terminals in dLGN (Figure S1C), as confirmed by co-labeling with presynaptic marker VGLUT2 (Figure 1A). While some colliculothalamic inputs express VGLUT2 (Cetin and Callaway, 2014), collicular neurons did not express ChR2 (Figure S1B). Therefore, YFP+ VGLUT2+ terminals are retinal in origin. We next looked for YFP in visual cortex (V1). While we found sparse neuronal, glial, and vascular labeling in V1, YFP+ cells amounted to just 0.38% of NeuN+ somas in layer 6, which send feedback projections to dLGN (Figure 1C). Importantly, YFP expression was absent in the corticothalamic (CT) bundle innervating dLGN (compare Figure S1C' to C'') and did not overlap with VGLUT1, a marker for CT inputs in dLGN (Figure 1B; Fujiyama et al., 2003), indicating no significant ChR2 expression in CT feedback projections to dLGN. Finally, YFP expression in dLGN did not overlap with NeuN or SMI32, a label of TC neuron proximal dendrites, suggesting no ChR2 expression in TC neurons (Figure S1D and S1E; Jaubert-Miazza et al., 2005). These results show that *Chx10-Cre;ChR2* mice selectively express ChR2 in RGC inputs in dLGN.

We took advantage of this mouse to re-examine RG convergence. Our lab has employed the fiber fraction (FF) method to characterize convergence of the RGS in slice: the contribution of a single RGC input to the overall retinal drive onto a TC neuron (amplitude of single fiber EPSC [SF]/maximal EPSC; Hooks and

Chen, 2006). Averaging the FF over a TC neuron population provides an unbiased estimate of connectivity and a tool for relative comparisons of convergence over different ages and conditions. Thus we compared the maximal and minimal synaptic responses obtained with e-stim versus optical stimulation (o-stim).

Parasagittal dLGN slices from *Chx10-Cre;ChR2* mice were prepared at P27–34 for whole-cell voltage-clamp TC neuron recordings (Figure 2A). These slices offered three ways to evoke RG EPSCs: (1) e-stim electrode positioned distally in the OT (electrical EPSC, “eEPSC,” our established approach; Figures 2B and 2C); (2) 470 nm LED light o-stim through an optic fiber placed over the distal OT (fiber EPSC, “fEPSC”; Figure 2B), and (3) full-field 470 nm o-stim through a 60 \times objective (objective EPSC, “oEPSC”; Figure 2C).

We first compared a TC neuron’s maximal eEPSC (0.2 ms, 400 μ A, black trace) to its oEPSC response (full-field, 1 ms, 83 mW/mm², blue trace). The oEPSC resembled the eEPSC in activation and decay kinetics, with a fast inward AMPAR component at -70 mV holding potential (HP) and both fast AMPAR and slower-activating and -decaying NMDAR currents at $+40$ mV HP (Figures 2D and S2B). Glutamate receptor antagonists fully blocked the oEPSC (Figure S2B), ruling out contribution of non-glutamatergic currents, and the ratio of AMPAR to NMDAR peak currents did not differ between eEPSCs and oEPSCs (Table S1). On average, the maximal peak amplitude of oEPSC exceeded that of eEPSC (median 1.71 times greater; Figure 2E and Table S1).

Our data suggest that full-field o-stim activates severed RGC axons that e-stim does not. However, oEPSC may overestimate total input, as ChR2 stimulation can aberrantly enhance

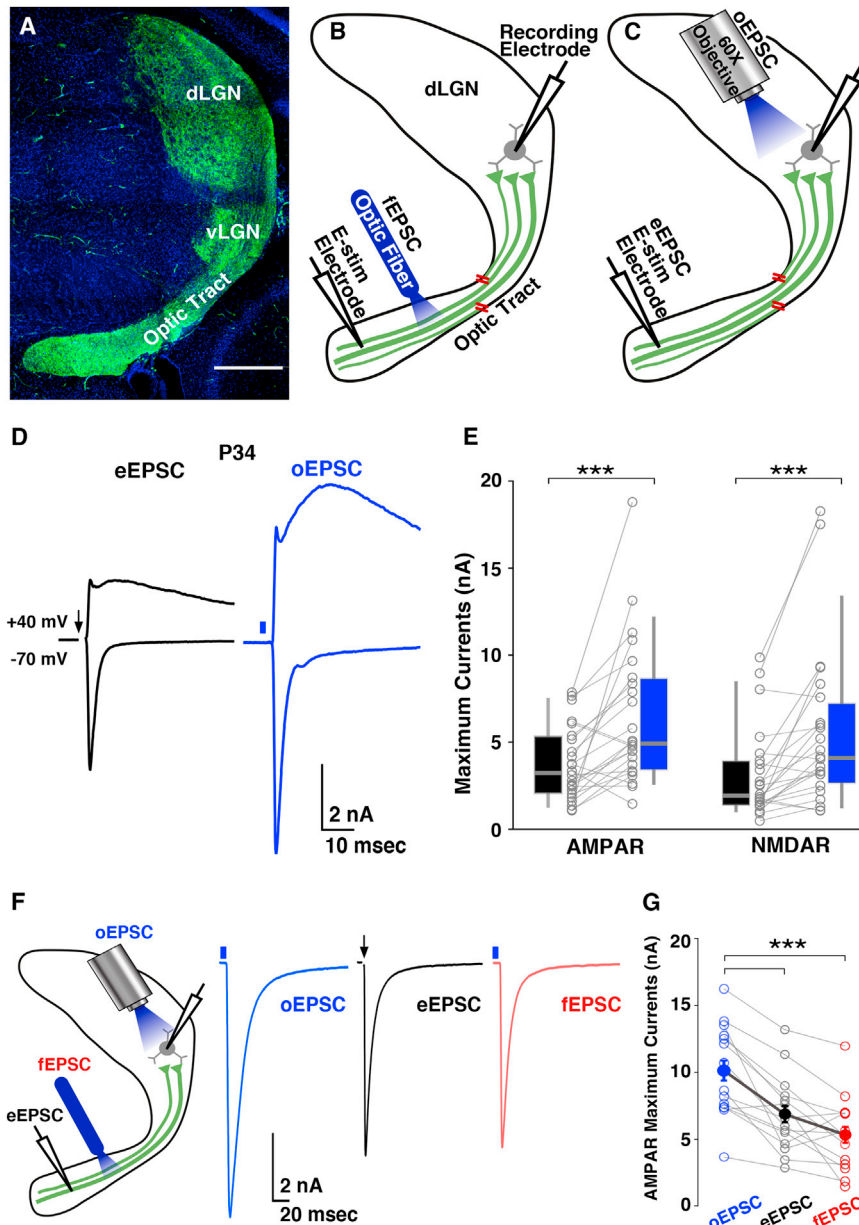


Figure 2. ChR2 Stimulation of Proximal RGC Axons Drives Larger Retinogeniculate Maximal Synaptic Currents than Optic Tract Stimulation

(A) Tiled confocal image of dLGN from *Chx10-Cre;ChR2* parasagittal slice.

(B and C) Schematic of stimulation paradigms used. Electrical stimulation evokes eEPSCs (e-stim electrode, B and C). 470-nm light stimulation via a 200- μ m-thick optic fiber positioned over the OT evokes fEPSC (B); via full-field illumination (60 \times objective) evokes maximal oEPSC (C). Red dashes indicate severed axons.

(D) Representative eEPSC (black) and oEPSC (blue) recordings from the same P34 TC neuron (HP +40 and -70 mV), as in (C). Black arrow and blue bar indicate e-stim and o-stim timing.

(E) Pairs of AMPAR (left) and NMDAR (right) maximal eEPSCs and oEPSCs recorded from $n = 24$ TC neurons (13 mice). Gray lines connect responses from the same neuron; boxplots summarize the population. For most cells, the oEPSC amplitude was larger. Box, 25%–75% IQR; whiskers, 10%–90% IQR.

(F) Comparison of full-field blue-light versus localized OT stimulations from the same cell. Left: Experimental schematic. Right: Maximal AMPAR oEPSC, eEPSC, and fEPSC from the same P29 neuron. Each trace averages 3–4 trials.

(G) Summary of AMPAR peak EPSCs from 13 cells/8 mice. Filled circles and black lines denote population averages with SEM (error bars); gray lines connect points from the same cell.

*** $p < 0.0001$. See also [Figure S2](#) and [Table S1](#) for detailed statistics.

presynaptic release (Jackman et al., 2014). Several controls argue against this explanation of our results. First, blocking action potential (AP)-driven release with TTX, a sodium channel inhibitor, abolished the oEPSC (Figure S2C; $n = 6$), indicating that activation of ChR2 channels alone does not drive transmitter release from RGC boutons. Second, comparison of the strength of oEPSC, eEPSC, and fEPSC from the same cell (with the optic fiber placed near the site of e-stim) showed that, like maximal eEPSCs, maximal fEPSCs were significantly smaller than oEPSCs (Figures 2F and 2G and Table S1). Third, there was no difference in the halfwidth of EPSCs (normalized to peak amplitude) evoked with these three stimulation modes (Table S1). These findings refute the scenario that ChR2 expression in axons broadens the AP waveform, prolonging transmitter release and

enhancing EPSCs. Accordingly, the response to pairs of pulses (paired-pulse ratio, PPR) of the oEPSCs resembled the maximal fEPSCs despite differences in strength, consistent with no effect of optogenetic stimulation on release probability (Figure S2D). Further, varying the duration of full-field o-stim (0.15–10 ms) did not alter PPR, amplitude, or decay kinetics of the oEPSC (Figures S2E–S2G). Together, these results show that activation of a greater number of RGC axon terminals, not ChR2-mediated enhancement of transmitter release, underlies the larger amplitude oEPSC.

ChR2 Stimulation Isolates Weak and Strong Single-Fiber Inputs

Single RG inputs can vary in strength from tens of pA to several nA, even in mature animals (Chen and Regehr, 2000). To determine whether the larger RG oEPSCs may arise from previously missed strong inputs or a range of weak and strong SFs, we adapted minimal e-stim protocols to optic fiber stimulation to assess the contribution of SF strengths to the oEPSC (Figure 3A; Noutel et al., 2011). Blue-light power was adjusted from ~ 0.5 to 10 mW/mm² across many trials to find the minimum intensity

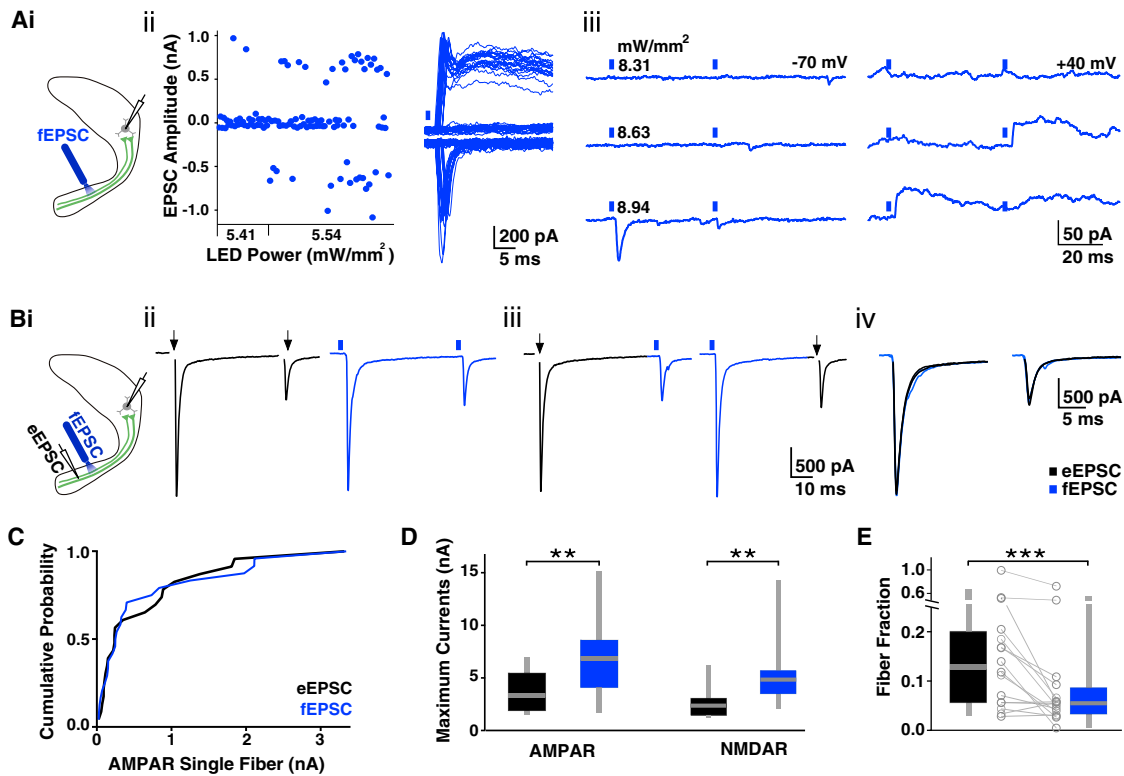


Figure 3. Isolation of Single Fibers with ChR2 Reveals Greater Convergence

(A) Optogenetic isolation of SF inputs. (i) Schematic for SF isolation using an optic fiber. (ii) Failures method: Multiple fEPSC trials recorded at HP -70 mV (inward currents) and $+40$ mV (outward currents) in response to two intensities of light. Probability of evoking an fEPSC was 8.7% at 5.41 mW/mm^2 (subthreshold) and increased to 49.3% at 5.54 mW/mm^2 (threshold), identifying a SF input. Left: Plot of peak EPSC amplitude versus trial number for the two intensities. Right: Overlaid traces evoked at 5.54 mW/mm^2 . (iii) Threshold method in another cell: Light intensity was increased gradually until the SF response became reliable while alternating trials at -70 (left) and $+40$ (right) mV HP. Two stimuli (separated by 50 ms) were used in each trial.

(B) Isolation of the same SF using o- and e-stim. (i) E-stim electrode and optic fiber o-stim in OT. (ii) The AMPAR EPSCs for both stimulus modes exhibit similar paired-pulse depression. (iii) Alternating o-stim (blue) and e-stim (black) in pairs of pulses shows interaction between the two stim responses, consistent with the activation of the same RGC axon. Traces average three trials. (iv) Overlaid responses to first (left) and second (right) stimulus from (ii) to (iii).

(C–E) Comparison of synaptic responses from P30 cells with at least one SF isolated by both o-stim and e-stim ($n = 16$). SF cumulative probability distribution (C, $p > 0.99$ Wilcoxon Signed Rank). Dataset is distinct from Figure 2E. (D) Maximal EPSCs. (E) Resulting Fiber Fraction (line connects oFF and eFF from the same cell). Box, 25%–75% IQR; whiskers, 10%–90% IQR.

** $p < 0.01$; *** $p < 0.001$. For detailed stats, see Table S2.

threshold. We primarily relied on the more efficient threshold method of SF isolation, although the $\sim 50\%$ failure method was also effective (Figure 3A and STAR Methods).

To verify that electrical and optic-fiber stimulation recruited the same RGC axon population, we took advantage of the characteristic RGS paired-pulse depression to attempt to activate the same afferent axonal input using o-stim and e-stim of the OT. While recording from a TC neuron, we could independently evoke a SF of similar amplitude and PPR when placing the optic fiber and e-stim pipette near one another in the OT (Figure 3Bi). If the eEPSC and fEPSC are evoked from two distinct RGC axons, then stimulating the eEPSC should not affect the amplitude of the subsequent fEPSC. If, however, they are evoked from the same axon, the second EPSC should reflect the previous short-term depression of that axon with any stimulus combination. Figure 3B shows a SF input with similar PPR regardless of stimulus order, indicating o-stim and e-stim recruit the same input. These results demonstrate that o-stim

and e-stim can be used interchangeably to isolate ChR2-expressing SF afferents.

The cumulative distributions of SF amplitudes isolated from 16 cells for which both optic fiber and e-stim identified a SF input (not necessarily the same input; Figure 3C) both span a range from tens of pA to nA and are statistically indistinguishable. A dataset expanded using cells where only one type of stimulation was used to isolate a SF also showed no difference ($n = 35$ – 36 SFs; $p = 0.94$ Mann-Whitney, MW). Our data therefore confirm that o-stim and e-stim recruit the same population of SF RGC axons and can both assess SF amplitude distribution.

Lower Fiber Fractions with O-Stim Reflect Higher Convergence

Our results demonstrate that o-stim measures the maximal retinal drive onto a given TC neuron more accurately by recruiting axons severed in slice. With this approach, we reassessed convergence at the murine RGS by comparing the FF ratio

(SF EPSC/max EPSC) of TC cells using e-stim and o-stim data shown in [Figures 3C and 3D](#). [Figure 3E](#) plots the pairs of electrical (eFF) and optical (oFF) fiber fractions calculated for these cells; the median eFF was 1.6 times larger than the oFF ([Table S2](#)). O-stim therefore identifies more inputs per TC neuron when compared to e-stim.

Simulation Identifies Many Weak, Few Strong RG Convergent Inputs

The FF was designed to compare RG convergence over different conditions ([Hooks and Chen, 2006](#)). However, it does not quantify the exact number of afferent inputs, as it disregards potential heterogeneity of SF strengths. We find the FF decreases with improvement in slice health, consistent with preservation of more RGC inputs ([Figure S3](#)). To estimate convergence in a manner that accounts for heterogeneity of input strengths, we implemented a simulation using our available datasets of oEPSC ([Figure 4A](#)) and e-stim- and o-stim-isolated SF current amplitudes ([Figure 4B](#)) from P30 mice ([STAR Methods](#)). A single trial of the “convergence simulation” consisted of two steps: (1) a maximal oEPSC amplitude is randomly chosen ([Figure 4A](#)), and (2) SF inputs are randomly chosen from the distribution ([Figure 4B](#)) and their amplitudes summed until the total reaches the chosen maximal. A total of 50,000 trials generated a population of simulated cells, for which we recorded the number and amplitude of SFs required to reach the maximal oEPSC amplitude ([Figures 4C and 4D](#)).

The simulation showed that 10.6 ± 6.5 (mean \pm 1 SD; SEM = 0.03, median = 9, IQR = 6–14) RGC inputs converge onto an average TC neuron ([Figure 4C](#)). Because strong SFs likely drive TC neuron spiking more effectively than weak SFs, we considered the relative strengths of converging inputs. First we defined the “threshold strength” as the peak AMPAR EPSC amplitude that can drive TC neuron spiking in response to one or a pair of OT pulses. We next plotted the number of SFs that exceed threshold for each simulation trial as a function of the threshold strength ([Figures 4E and 4F](#)). A prior *in vitro* study showed that RG threshold strength is 600 pA at P30 ([Liu and Chen, 2008](#), HP = –55 mV). Applying this threshold to our simulated results revealed that of the \sim 10.6 inputs that innervated a TC neuron, 3.2 ± 1.9 (mean \pm 1 SD; median = 3, IQR = 2–4) were “strong” inputs ($>$ 600 pA, [Figure 4D](#), dotted line), whereas 7.4 ± 5.3 (mean \pm 1 SD; median = 6, IQR = 3–10) inputs were “weak” ($<$ 600 pA). Therefore, on average, \sim 30% of inputs to a TC neuron were strong enough to reliably drive AP firing.

Many RGC Inputs Are Functionally Eliminated over Development

The observation of higher convergence than previously estimated in P30 mice raised the question of whether developmental RG refinement occurs ([Hammer et al., 2015](#)). Indeed, the low mean oFF (0.097) is similar to previously reported immature eFF (\sim 0.1, [Hooks and Chen, 2006](#)). Yet these values cannot be directly compared because, as shown here, ChR2 stimulation captures substantially more inputs than e-stim. Unfortunately, we cannot directly compare oFF across ages: despite embryonic onset of Chx10-Cre expression ([Rowan and Cepko, 2004](#)), ChR2 expression is not sufficiently homogeneous to accurately measure maximal EPSCs in slices from immature (P9–16) mice ([Fig-](#)

[ures S4A–S4C and Table S3](#)) until after the bulk of refinement has occurred ($>$ P16, [Hooks and Chen, 2006](#)). Therefore, we compared eFF over age by recording a new P9 dataset under the same slicing conditions as the P30 data shown above ([Figure S3](#)). As in previous reports, immature SF amplitude distributions grossly favored the very weak, and the eFF was considerably smaller at P9 than at P30 or P60 ([Figures S4D and S4F and Tables S2 and S4](#)). The FF thus remains a robust tool for comparing convergence across different conditions.

We also utilized the P9 SF and maximal eEPSC datasets in the convergence simulation. This simulation yielded an average of 33 ± 20 (mean \pm 1 SD; median = 28, IQR = 20–40) inputs per P9 neuron. Despite not accounting for inputs from severed axons, the simulated convergence at P9 is still substantially greater than our optical estimates at P30 ([Figure 4G](#)). Therefore, our results confirm that developmental refinement does occur at the RG synapse, with more than a 3-fold reduction in RG convergence over development.

DISCUSSION

Structure versus Function of the RGS

We report functional RG convergence that is greater than previously appreciated in mice ([Chen and Regehr, 2000](#); [Jaubert-Miazza et al., 2005](#); [Lee et al., 2014](#); [Stevens et al., 2007](#)), but well below recent estimates from EM connectomics and retrograde rabies tracing studies of the mouse dLGN (40–91 RGC inputs; [Morgan et al., 2016](#); [Rompani et al., 2017](#)). This discrepancy may reflect the natural progression of functional refinement between the ages of P9 and P60, when synapse elimination precedes axon retraction by many weeks ([Chen and Regehr, 2000](#); [Hong et al., 2014](#)). Regional differences in binocular ([Rompani et al., 2017](#)) and monocular (present study) dLGN zones studied may also explain the inconsistency in numbers. Furthermore, [Morgan et al. \(2016\)](#) point out that they may overestimate convergence by a factor of 2 or 3 due to potential axon branching at the level of the OT. Finally, high-resolution ultrastructural analysis does not account for presynaptic release probability and would benefit from quantification of postsynaptic receptors to assess functional relevant morphological contacts. Altogether, our results highlight that synergy between functional analysis and connectomics is critical for understanding even a simple “relay” circuit.

Evidence for Heterogeneity of RG Input Strengths across Species

While we find \sim 10 convergent RGC inputs in P30 mice, our simulation shows that only a third of these inputs are strong enough to independently drive TC neuron spiking ([Figures 4E and 4F](#)). The heterogeneity of SF RGC inputs is not just a transient byproduct of development, as the distribution of SF input strength does not change significantly between P30 and $>$ P60 ([Table S4](#)). Our simulation assumes randomness in convergent inputs to provide the most unbiased outcome. Alternative constrained wiring patterns were also considered, but their simulation results did not yield a closer match to experimental observations ([STAR Methods](#)). More rules of RGC convergence may emerge in future research to refine this model, although we

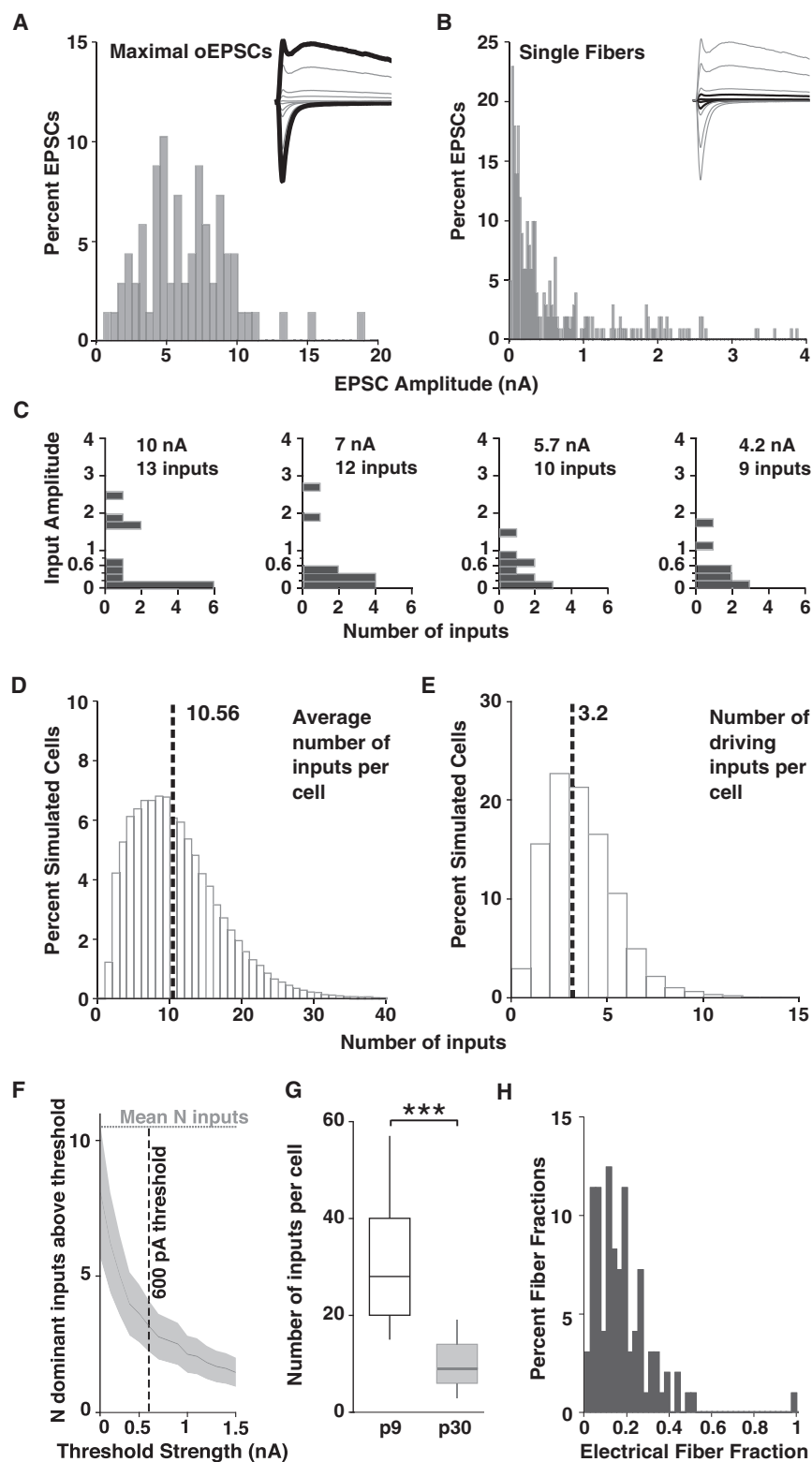


Figure 4. Simulation of Retinogeniculate Convergence

(A and B) Data input: histogram distributions of max oEPSC amplitudes ($n = 68$, P30, this study) (A) and P30 SFs ($n = 271$) combined from this and other (Figure 4J in [Hong et al., 2014](#); unpublished C57 experiments) studies. (B). Insets: bold traces show data type plotted.

(C) Example distributions of synaptic strengths for all inputs of four simulated cells.

(D and E) Histogram distributions of 50,000 simulated cells for (D) average number of inputs (median = 9, IQR = 6–14) and (E) average number of dominant inputs exceeding 600 pA (median = 3, IQR = 2–4). Black dashed line indicates the mean. (F) The number of dominant inputs as a function of changing the threshold strength (mean \pm 1/2 SD; bin size = 100 pA).

(G) Simulation results for number of inputs at P9 versus P30. *** $p < 0.001$ MW. Box, 25%–75% IQR; whiskers, 10%–90% IQR.

(H) FF histogram plot combining e-stim data from this study with that of [Thompson et al., 2016](#) (P30, $n = 96$).

See also [Figures S3 and S4](#).

believe the cumulative population of SFs reflects the statistics of RG input strengths.

Comparison of RG convergence across species reveals common themes. *In vivo* recordings that correlate spiking activity of RGC-TC neuron pairs in cats and primates report one or several dominant RGCs that drive TC neuron firing (Cleland et al., 1971; Hubel and Wiesel, 1961; Mastronarde, 1992; Sincich et al., 2007; Yeh et al., 2009). However, additional weaker inputs were also found in cat, and notably, most RGCs drive < 50% (range 1%–82%) of the postsynaptic spiking of both X and Y neurons (Rathbun et al., 2016; Usrey et al., 1999). These findings are in agreement with the broad distribution of the SF population we show *in vitro* in mice here and previously (Chen and Regehr, 2000). The *in vivo* results are also consistent with the landmark cat EM study often used to argue for low convergence based on a single reconstructed X-RGC axon arbor that provided the only retinal input to one TC X-cell (Hamos et al., 1987). However, only 20% of the entire arbor was reconstructed, and this section also innervated three other TC neurons. Thus the full axon may have diverged onto ~20 LGN neurons. As TC-X cells outnumber X-RGCs by more than 2-fold, this divergence predicts a RG convergence much greater than 1.

Importantly, convergence differs among information streams in the cat, where TC Y-cells receive more RGC inputs (~10 inputs) than X-cells (Robson, 1993; Weyand 2016). In mice, functional distinctions between TC neuron types are still debated (Krahe et al., 2011; Denman and Contreras, 2016), and distinct convergence modes were not obvious in our analysis of >90 FFs (Figure 4H). It is unlikely that we are conflating separate populations that exhibit low versus high degree of convergence, as we often isolate both a strong and a weak SF input onto the same TC neuron. However, it is possible that our experimental conditions constrained analysis to subpopulations of dLGN TC neurons. Finally, work in the koniocellular TC neurons of marmosets showing orientation selectivity and binocular convergence suggests that primate TC neurons can also support the integration of multiple RGC inputs (Cheong et al., 2013). Our findings in mice, therefore, are consistent with the literature showing that RGC inputs that dominate TC neuron firing can represent a subset of a larger number of convergent inputs in other mammals. Differences in the exact number of convergent inputs and the relative weights of weak and strong inputs may distinguish mice from other species.

Implications of Convergence

Our findings lend support to a shift in conceptualizing the dLGN as a complex network rather than a simple relay (Marshall et al., 2012; Piscopo et al., 2013; Scholl et al., 2013; Zhao et al., 2013). Using rabies tracing, Rompani et al., (2017) detected convergence of putative contacts from anatomically distinct RGCs. Whether these contacts are functional is still not known, but the observation suggests that converging inputs of different RGC subtypes may generate novel receptive field features in dLGN, adding a new dimension to thalamic processing. A more nuanced view of the dLGN informs more broadly the role of thalamic circuits in complex sensory and cognitive processes (Litvina and Chen, 2017; Schmitt and Halassa, 2017).

The functional role of weak RGC inputs in adult mice and other species remains unclear. We find no clear separation between populations of strong and weak inputs at any level of analysis, suggesting a continuity of functional relevance. While the threshold strength is 600 pA for single or pairs of EPSCs to drive TC neuron firing *in vitro*, weaker inputs may contribute to TC spiking when active alongside strong inputs or under modulated conditions that change the membrane resistance (Figure 4F). Converging weak inputs could synchronize the activity of groups of dLGN neurons, providing effective coincident stimuli for cortical activation (Alonso et al., 2006). They may also improve signal-to-noise in thalamic circuits to enhance perceptual acuity, create novel receptive fields that increase the continuity in visual or temporal space, or form novel feature detectors absent in the retina (Martinez et al., 2014; Usrey and Alitto, 2015). Finally, small inputs may support adult plasticity of RG connectivity through changes in synaptic weight (Litvina and Chen, 2017). Indeed, cat and primate TC neurons exhibit rapid plasticity in receptive field properties in response to acute perturbation of RGC or cortical input activity, as well as changes in brain state (Aguila et al., 2017; Hei et al., 2014; Moore et al., 2011). Thus the convergence of RGC inputs with varying strengths may enable plasticity of visual information transfer, which could eventually serve as a tool for correcting circuit defects secondary to development or disease.

STAR★METHODS

Detailed methods are provided in the online version of this paper and include the following:

- KEY RESOURCES TABLE
- CONTACT FOR REAGENT AND RESOURCE SHARING
- EXPERIMENTAL MODEL AND SUBJECT DETAILS
 - Animals
- METHOD DETAILS
 - Slice Preparation
 - Comparison of Cutting Solutions
 - Tissue Preparation and Immunohistochemistry
 - Microscopy
 - Electrophysiology and Optical Stimulation
 - Single Fiber Stimulation
 - Convergence Simulation
 - Experimental Design
- QUANTIFICATION AND STATISTICAL ANALYSIS
 - Image Quantification
 - Data Analysis and Statistics
 - Fiber Fraction Assessment

SUPPLEMENTAL INFORMATION

Supplemental Information includes four figures and four tables and can be found with this article online at <https://doi.org/10.1016/j.neuron.2017.09.037>.

AUTHOR CONTRIBUTIONS

E.Y.L. conducted all experiments, analyzed data, and prepared figures. E.Y.L. and C.C. designed research, interpreted results, and prepared and approved the manuscript.

ACKNOWLEDGMENTS

The authors thank all Chen lab members for helpful discussions on the experiments and manuscript; S. Curtiss, G. Rankin, M. Taylor, and J. Lefler for technical assistance; M. Do, W. Regehr, and T. Schwarz for comments on the study; C. Cepko for the Chx10-Cre line; IDDRRC Imaging Core, supported by NIH U54 HD090255; and T. Hill for assistance with confocal imaging. This work was supported by NIH R01EY013613 to C.C. and the Edward R. and Anne G. Lefler Predoctoral Fellowship to E.Y.L.

Received: June 16, 2017

Revised: September 1, 2017

Accepted: September 22, 2017

Published: October 11, 2017

REFERENCES

- Aguila, J., Cudeiro, F.J., and Rivadulla, C. (2017). Suppression of V1 Feedback Produces a Shift in the Topographic Representation of Receptive Fields of LGN Cells by Unmasking Latent Retinal Drives. *Cereb. Cortex* *27*, 3331–3345.
- Alonso, J.M., Yeh, C.I., Weng, C., and Stoelzel, C. (2006). Retinogeniculate connections: A balancing act between connection specificity and receptive field diversity. *Prog. Brain Res.* *154*, 3–13.
- Cetin, A., and Callaway, E.M. (2014). Optical control of retrogradely infected neurons using drug-regulated “TLoop” lentiviral vectors. *J. Neurophysiol.* *111*, 2150–2159.
- Chen, C., and Regehr, W.G. (2000). Developmental remodeling of the retinogeniculate synapse. *Neuron* *28*, 955–966.
- Cheong, S.K.K., Tailby, C., Solomon, S.G., and Martin, P.R. (2013). Cortical-like receptive fields in the lateral geniculate nucleus of marmoset monkeys. *J. Neurosci.* *33*, 6864–6876.
- Cleland, B.G., Dubin, M.W., and Levick, W.R. (1971). Simultaneous recording of input and output of lateral geniculate neurones. *Nat. New Biol.* *231*, 191–192.
- Denman, D.J., and Contreras, D. (2016). On Parallel Streams through the Mouse Dorsal Lateral Geniculate Nucleus. *Front. Neural Circuits* *10*, 20.
- Fujiyama, F., Hioki, H., Tomioka, R., Taki, K., Tamamaki, N., Nomura, S., Okamoto, K., and Kaneko, T. (2003). Changes of immunocytochemical localization of vesicular glutamate transporters in the rat visual system after the retinofugal denervation. *J. Comp. Neurol.* *465*, 234–249.
- Hammer, S., Monavarfeshani, A., Lemon, T., Su, J., and Fox, M.A. (2015). Multiple Retinal Axons Converge onto Relay Cells in the Adult Mouse Thalamus. *Cell Rep.* *12*, 1575–1583.
- Hamos, J.E., Van Horn, S.C., Raczkowski, D., and Sherman, S.M. (1987). Synaptic circuits involving an individual retinogeniculate axon in the cat. *J. Comp. Neurol.* *259*, 165–192.
- Hauser, J.L., Edson, E.B., Hooks, B.M., and Chen, C. (2013). Metabotropic glutamate receptors and glutamate transporters shape transmission at the developing retinogeniculate synapse. *J. Neurophysiol.* *109*, 113–123.
- Hei, X., Stoelzel, C.R., Zhuang, J., Bereshpolova, Y., Huff, J.M., Alonso, J.M., and Swadlow, H.A. (2014). Directional selective neurons in the awake LGN: response properties and modulation by brain state. *J. Neurophysiol.* *112*, 362–373.
- Hong, Y.K., Park, S., Litvina, E.Y., Morales, J., Sanes, J.R., and Chen, C. (2014). Refinement of the retinogeniculate synapse by bouton clustering. *Neuron* *84*, 332–339.
- Hooks, B.M., and Chen, C. (2006). Distinct roles for spontaneous and visual activity in remodeling of the retinogeniculate synapse. *Neuron* *52*, 281–291.
- Hooks, B.M., and Chen, C. (2008). Vision triggers an experience-dependent sensitive period at the retinogeniculate synapse. *J. Neurosci.* *28*, 4807–4817.
- Hubel, D.H., and Wiesel, T.N. (1961). Integrative action in the cat’s lateral geniculate body. *J. Physiol.* *155*, 385–398.
- Jackman, S.L., Beneduce, B.M., Drew, I.R., and Regehr, W.G. (2014). Achieving high-frequency optical control of synaptic transmission. *J. Neurosci.* *34*, 7704–7714.
- Jaubert-Miazza, L., Green, E., Lo, F.-S., Bui, K., Mills, J., and Guido, W. (2005). Structural and functional composition of the developing retinogeniculate pathway in the mouse. *Vis. Neurosci.* *22*, 661–676.
- Krahe, T.E., El-Danaf, R.N., Dilger, E.K., Henderson, S.C., and Guido, W. (2011). Morphologically distinct classes of relay cells exhibit regional preferences in the dorsal lateral geniculate nucleus of the mouse. *J. Neurosci.* *31*, 17437–17448.
- Lee, H., Brott, B.K., Kirkby, L.A., Adelson, J.D., Cheng, S., Feller, M.B., Datwani, A., and Shatz, C.J. (2014). Synapse elimination and learning rules co-regulated by MHC class I H2-Db. *Nature* *509*, 195–200.
- Litvina, E.Y., and Chen, C. (2017). An evolving view of retinogeniculate transmission. *Visual Neuroscience* *34*, E013.
- Liu, X., and Chen, C. (2008). Different roles for AMPA and NMDA receptors in transmission at the immature retinogeniculate synapse. *J. Neurophysiol.* *99*, 629–643.
- Madisen, L., Mao, T., Koch, H., Zhuo, J.M., Berenyi, A., Fujisawa, S., Hsu, Y.-W., Garcia, A.J., 3rd, Gu, X., Zanella, S., et al. (2012). A toolbox of Cre-dependent optogenetic transgenic mice for light-induced activation and silencing. *Nat. Neurosci.* *15*, 793–802.
- Marshall, J.H., Kaye, A.P., Nauhaus, I., and Callaway, E.M. (2012). Anterior-posterior direction opponency in the superficial mouse lateral geniculate nucleus. *Neuron* *76*, 713–720.
- Martinez, L.M., Molano-Mazón, M., Wang, X., Sommer, F.T., and Hirsch, J.A. (2014). Statistical wiring of thalamic receptive fields optimizes spatial sampling of the retinal image. *Neuron* *81*, 943–956.
- Mastrorade, D.N. (1992). Nonlagged relay cells and interneurons in the cat lateral geniculate nucleus: receptive-field properties and retinal inputs. *Vis. Neurosci.* *8*, 407–441.
- Moore, B.D., 4th, Kiley, C.W., Sun, C., and Usrey, W.M. (2011). Rapid plasticity of visual responses in the adult lateral geniculate nucleus. *Neuron* *71*, 812–819.
- Morgan, J.L., Berger, D.R., Wetzel, A.W., and Lichtman, J.W. (2016). The Fuzzy Logic of Network Connectivity in Mouse Visual Thalamus. *Cell* *165*, 192–206.
- Noutel, J., Hong, Y.K., Leu, B., Kang, E., and Chen, C. (2011). Experience-dependent retinogeniculate synapse remodeling is abnormal in MeCP2-deficient mice. *Neuron* *70*, 35–42.
- Piscopo, D.M., El-Danaf, R.N., Huberman, A.D., and Niell, C.M. (2013). Diverse visual features encoded in mouse lateral geniculate nucleus. *J. Neurosci.* *33*, 4642–4656.
- Pressler, R.T., and Regehr, W.G. (2013). Metabotropic glutamate receptors drive global persistent inhibition in the visual thalamus. *J. Neurosci.* *33*, 2494–2506.
- Rathbun, D.L., Alitto, H.J., Warland, D.K., and Usrey, W.M. (2016). Stimulus Contrast and Retinogeniculate Signal Processing. *Front. Neural Circuits* *10*, 8.
- Robson, J.A. (1993). Qualitative and quantitative analyses of the patterns of retinal input to neurons in the dorsal lateral geniculate nucleus of the cat. *J. Comp. Neurol.* *334*, 324–336.
- Rompani, S.B., Müllner, F.E., Wanner, A., Zhang, C., Roth, C.N., Yonehara, K., and Roska, B. (2017). Different Modes of Visual Integration in the Lateral Geniculate Nucleus Revealed by Single-Cell-Initiated Transsynaptic Tracing. *Neuron* *93*, 767–776.e6.
- Rowan, S., and Cepko, C.L. (2004). Genetic analysis of the homeodomain transcription factor Chx10 in the retina using a novel multifunctional BAC transgenic mouse reporter. *Dev. Biol.* *271*, 388–402.
- Schmitt, L.J., and Halassa, M.M. (2017). Interrogating the mouse thalamus to correct human neurodevelopmental disorders. *Mol. Psychiatry* *22*, 183–191.

- Scholl, B., Tan, A.Y.Y., Corey, J., and Priebe, N.J. (2013). Emergence of orientation selectivity in the Mammalian visual pathway. *J. Neurosci.* *33*, 10616–10624.
- Sincich, L.C., Adams, D.L., Economides, J.R., and Horton, J.C. (2007). Transmission of spike trains at the retinogeniculate synapse. *J. Neurosci.* *27*, 2683–2692.
- Stevens, B., Allen, N.J., Vazquez, L.E., Howell, G.R., Christopherson, K.S., Nouri, N., Micheva, K.D., Mehalow, A.K., Huberman, A.D., Stafford, B., et al. (2007). The classical complement cascade mediates CNS synapse elimination. *Cell* *131*, 1164–1178.
- Thompson, A.D., Picard, N., Min, L., Fagiolini, M., and Chen, C. (2016). Cortical Feedback Regulates Feedforward Retinogeniculate Refinement. *Neuron* *91*, 1021–1033.
- Usrey, W.M., and Alitto, H.J. (2015). Visual Functions of the Thalamus. *Annu Rev Vis Sci* *1*, 351–371.
- Usrey, W.M., Reppas, J.B., and Reid, R.C. (1999). Specificity and strength of retinogeniculate connections. *J. Neurophysiol.* *82*, 3527–3540.
- Weyand, T.G. (2016). The multifunctional lateral geniculate nucleus. *Rev. Neurosci.* *27*, 135–157.
- Yeh, C.-I., Stoelzel, C.R., Weng, C., and Alonso, J.M. (2009). Functional consequences of neuronal divergence within the retinogeniculate pathway. *J. Neurophysiol.* *101*, 2166–2185.
- Zhao, X., Chen, H., Liu, X., and Cang, J. (2013). Orientation-selective responses in the mouse lateral geniculate nucleus. *J. Neurosci.* *33*, 12751–12763.

STAR★METHODS

KEY RESOURCES TABLE

REAGENT or RESOURCE	SOURCE	IDENTIFIER
Antibodies		
Chicken anti-GFP	Aves Labs	Cat# GFP-1020; RRID: AB_10000240
Guinea-pig anti-VGLUT1	Millipore	Cat# AB5905; RRID: AB_2301751
Guinea-pig anti-VGLUT2	Millipore	Cat# AB2251; RRID: AB_1587626
Mouse anti-SMI32	Biologend	Cat# 801701; RRID: AB_2564642
Mouse anti-NeuN	Millipore	Cat# MAB377; RRID: AB_2298772
Alexa 488 Goat anti-Chicken	Thermo Fisher Scientific	Cat# A-11039; RRID: AB_2534096
Alexa 555 Goat anti-Guinea-pig	Thermo Fisher Scientific	Cat# A-21435; RRID: AB_2535856
Alexa 555 Donkey anti-mouse	Thermo Fisher Scientific	Cat# A-31570; RRID: AB_2536180
DAPI	Sigma Aldrich	Cat# D9542
Chemicals, Peptides, and Recombinant Proteins		
Bicuculline	Tocris	Cat# 0130
CPP	Tocris	Cat# 0247
LY341495	Tocris	Cat# 1209
CGP55845	Tocris	Cat # 1248
DPCPX	Tocris	Cat# 0439
NBQX	Tocris	Cat# 0373
Cyclothiazide	Tocris	Cat# 0713
Critical Commercial Assays		
VECTASHIELD Mounting Medium with DAPI	Vector Laboratories	Cat#: H-1500; RRID: AB_2336788
Experimental Models: Organisms/Strains		
Chx10-Cre mouse Tg(Chx10-EGFP/cre,-ALPP)2Clc/J	Cepko Lab	JAX 005105; RRID: MGI:3052551
Ai32 ChR(H134R)-EYFP mouse B6;129S-Gt(ROSA) 26Sor ^{tm32(CAG-COP4*H134R/EYFP)Hze/J}	Jackson	JAX 012569
C57BL/6J mouse	Jackson	RRID: IMSR_JAX:000664
Software and Algorithms		
Fiji/ImageJ 2.0.0-rc-59/1.51n	NIH	ImageJ; RRID: SCR_003070
MATLAB R2016b	Mathworks	https://www.mathworks.com/products/matlab.html ; RRID: SCR_001622
Igor Pro 6.12	Wavemetrics	https://www.wavemetrics.com/products/igorpro/igorpro.htm ; RRID: SCR_000325
JMP Pro 12.0.1	SAS Institute Inc	https://www.jmp.com/en_us/home.html
Other		
CoolLED 470 nm light sources pE-100 and pE-100 ^{fiber}	Scientifica	http://www.cooled.com/product-detail/pe-100/
200 μ m, 0.39 nA Optic Fiber	Thorlabs	Cat # M38L02

CONTACT FOR REAGENT AND RESOURCE SHARING

Further information and requests for resources and reagents should be directed to and will be fulfilled by the Lead Contact, Chinfai Chen (chinfai.chen@childrens.harvard.edu).

EXPERIMENTAL MODEL AND SUBJECT DETAILS

Animals

All animal procedures were in compliance with the NIH Guide for the Care and Use of Laboratory Animals and approved by the Institutional Animal and Care and Use Committee (IACUC) at Boston Children's Hospital. Male and female animals aged P27-34 were included in the "P30" category, P60-100 in "P60," and P9-10 C57BL/6J wild-type (WT) in "P9." All mice were group (up to 5 adults per cage) housed in Optimice (Animal Care Systems) cages with Biofresh bedding on a 12 hr light/dark cycle with a diet of Prolab Isopro RMH 3000 (LabDiet) and deionized, UV-sterilized water obtained through reverse osmosis. To drive the expression of ChR2 expression in RGCs, homozygous *Chx10-Cre* mice (Rowan and Cepko, 2004; JAX 005105) were crossed with homozygous Ai32 mice (Madisen et al., 2012; JAX # 012569) yielding progeny heterozygous for each gene and expressing ChR2 in the RGCs and other layers of the retina ("*Chx10-Cre;ChR2*"). In Ai32 mice, a STOP cassette flanked by two loxP sites separates the CAG promoter from the *ChR2(H134R)-EYFP* gene. We chose a transgenic strategy over viral-mediated infection to avoid damaging the retina, and to reduce variability of ChR2 expression level between RGCs and between mice. Viral vectors may also distort presynaptic release, confounding a quantitative analysis of retinogeniculate convergence (Jackman et al., 2014).

METHOD DETAILS

Slice Preparation

Brain slices containing the optic tract (OT) and dLGN were obtained from *Chx10-Cre;ChR2* or C57BL/6J (P9-10, "P9") mice as previously described (Chen and Regehr, 2000). This established parasagittal slice preparation preferentially preserves connectivity between RGC axons that can be stimulated in the optic tract and dLGN neurons in the monocular zone of the dLGN. Mice were anesthetized with isoflurane; after decapitation the head was cooled, the brain was removed and immersed into oxygenated ice-cold cutting solution containing (in mM): 130 mM K-gluconate, 15 mM KCl, 0.05 mM EGTA, 20 mM HEPES, and 25 mM glucose (pH 7.4) with NaOH (Pressler and Regehr, 2013; Hong et al., 2014). This cutting solution improves viability of slices from mice up to and older than p100. 250 μ m-thick slices were cut in this solution using a sapphire blade (Delaware Diamond Knives, Wilmington, DE) on a vibratome (VT1200S; Leica, Deerfield, IL) and were allowed to recover at 31°C for 20-25 mins and at room temperature for an additional 10-15 mins in oxygenated saline solution (in mM: 125 NaCl, 26 NaHCO₃, 1.25 NaH₂PO₄, 2.5 KCl, 1.0 MgCl₂, 2.0 CaCl₂, and 25 glucose (Sigma) adjusted to 310-315 mOsm).

Comparison of Cutting Solutions

In this study we use data from prior publications to track improvements in slice health. Figure S3 summarizes data combined from several previous publications from our lab. With improvements in the slice preparation and cutting solution techniques across our previously published studies, we noticed a decline in fiber fractions (Figure S3C) that aligned with increased number of live cells in the slice and an experience of longer-lasting, more stable recordings.

All datasets are comprised of recordings from dLGN slices of P27-34 C57BL/6J-background WT animals prepared with different cutting solutions. The "Choline" cutting solution, which replaced 25% of sodium with choline, was used in Hooks and Chen (2006), Figures 4, 5, and 6, and Noutel et al., 2011, Figure 2: (mM) NaCl 78.3, NaHCO₃ 23, glucose 23, choline chloride 33.8, KCl 2.3, NaH₂PO₃ 1.1, MgCl₂ 6.4, CaCl 0.45. The "Enhanced Choline" solution, which replaced 73% sodium concentration with choline, and added 3.1mM sodium pyruvate and 11.6mM sodium ascorbate, was used in Thompson et al., 2016: choline chloride 110, sodium pyruvate 3.1, sodium ascorbate 11.6, NaHCO₃ 25, glucose 25, MgCl₂ 7, KCl 2.5, NaH₂PO₄ 1.25, CaCl₂ 0.5. The "K-Gluconate" solution, which replaced 100% of sodium with potassium gluconate, was used in Hong et al., 2014: 130, KCl 15, EGTA 0.05, HEPES 20, glucose 25 pH 7.4. Maximal peak AMPAR or NMDAR EPSC amplitudes were more than doubled in the healthier slices (Figure S3B), while the distributions of SF EPSC peak amplitudes remained constant across cutting conditions (Figure S3A), indicating that the improved solutions are not causing retinal axon sprouting or non-specific changes in postsynaptic glutamatergic receptors. Therefore, the enhanced cutting solutions preserve both cell integrity and more of the severed retinal axons, leading to increased maximal currents and a higher estimate of retinogeniculate convergence.

Tissue Preparation and Immunohistochemistry

Tissue for Figures 1 and S1 was prepared from *Chx10-Cre;ChR2* brains and retinae preserved by transcardial perfusion with 4% PFA, post-fixed in 4% PFA overnight and infiltrated with 30% sucrose in 0.1 mM phosphate buffer before sectioning. 60 μ m-thick coronal free-floating sections were prepared from perfused brains on a Leica VT1000 vibratome, and retinae for Figure S1 were sectioned on a cryostat Leica CM3050S at 16 μ m thickness and mounted onto slides (VWR Superfront Plus, 48311-703). The parasagittal slice from an *in vitro* electrophysiology experiment shown in Figure 2A was incubated in 4% PFA for 20 mins after the experiment and stored in PBS until immunohistochemistry was performed. Standard fluorescent immunohistochemistry protocols were used, as previously described (Hong et al., 2014; Thompson et al., 2016). Immunohistochemistry was performed for GFP (Chicken anti GFP, AVES GFP-1020 1:1000) on all imaged tissue. The following antibodies were used: Guinea-pig anti VGLUT1 (1:1000 AB5905, Millipore, MA) Guinea-pig anti-VGLUT2 (1:2000 AB2251 Millipore, MA), mouse anti SMI32 (1:1000, Biolegend 801701), and mouse anti NeuN (1:1000, Millipore MAB 377). Secondary antibodies were all used at 1:1000 concentration (Life Technologies/Invitrogen): goat

anti chicken 488 (A11039), goat anti GP 555 (A21435), donkey anti mouse 555 (A31570). Tissue was then incubated with DAPI for nuclear detection, mounted, and coverslipped with Vectashield (VectorLabs).

Microscopy

Confocal microscopy was carried out on Zeiss LSM 700 or 710 microscopes equipped with 5x-60x objectives, as described in Hong et al., 2014. Tiling (Figure 2A) was automated with built-in functions in Zeiss imaging software on the LSM 710. For quantification of V1 *Chx10:ChR2* (YFP) labeling, tiled Z stacks of YFP and NeuN signal in 60 μ m-thick sections of V1 were acquired on the Nikon Ti Eclipse inverted microscope using a 10x objective.

Electrophysiology and Optical Stimulation

Whole-cell voltage clamp recordings of TC neurons were performed as previously described using glass pipettes (1–2.0 M Ω) filled with an internal solution consisting of (in mM): 35 CsF, 100 CsCl, 10 EGTA, 10 HEPES, and the L-type calcium channel antagonist, 0.1 methoxyverapamil (290–300 mOsm, pH 7.3; Sigma). All experiments were performed at room temperature in oxygenated saline solution containing 20 μ M GABA_A receptor antagonist bicuculline (20 μ M; Tocris, Ellisville, MO). In addition to bicuculline, for experiments that were designed to compare the amplitude, time course, and paired-pulse properties of maximal eEPSCs, oEPSCs, and fEPSCs (those presented in Figures 2F and 2G, S2D–S2F), the following drugs were included in the bath: 50 μ M cyclothiazide to block AMPAR desensitization, 20 μ M CPP to block NMDAR currents, 10 μ M DPCPX to block A1 adenosine receptors, 50 μ M LY341495 to block presynaptic mGluRs (Hauser et al., 2013), and 2 μ M CGP55845 to block GABA_B. For EPSC amplitudes less than 20 pA, we frequently average 3–5 trials to measure the amplitude of single fiber inputs. With baseline RMS noise of 2–3 pA in single trial raw recordings, we are able to resolve synaptic currents of 10 pA and greater, and down to 6 pA by averaging multiple trials. Since our previous electrical stimulation studies were performed in the monocular zone, where connectivity between RGC axons in the optic tract and dLGN neurons are better preserved when compared to the ipsilateral patch, we limited our TC recordings in this current study to the same region.

Experiments designed to assess the development of ChR2 expression using NMDAR currents (Figures S4A–C) were performed in the presence of bicuculline along with 2 μ M CGP55845, 10 μ M DPCPX, and 5 μ M NBQX to block AMPAR currents.

Three types of axonal stimulation were used in this study, as described in Figure 2. For electrical stimulation (to evoke an “eEPSC”), a pair of electrodes, filled with saline solution, was placed in the OT in a location that optimized the maximal evoked current. Electrical stimuli were 0.25 ms in duration and ranged in amplitude from 5–400 μ A (100–400 μ A stimuli were used to obtain the maximal eEPSC response, WPI A365). For optical stimulation of the ChR2-expressing OT bundle at a distance (> 600 μ m) from the axonal terminals (to evoke an “fEPSC”), a 200 μ m-thick optic fiber, 0.39nA (Thorlabs) was threaded through the barrel of a glass pipette; the center of the resulting elliptical \sim 1mm² spot of 470nm blue light (0.5 \times 0.7 mm) was positioned over a similar location in the OT as electrical stimulation. 470nm illumination was provided by a CoolLED pE-100^{fiber} system for this fiber (Max light intensity through fiber: 49 mW/mm² (Scientifica)). Optic fiber stimuli ranged from 1–4 ms in duration and from \sim 0.5–49 mW/mm² in intensity; the maximal intensity was always used to obtain the maximal fEPSC. For full-field stimulation that evoked a maximal ChR2-mediated EPSC (the “oEPSC”), a second CoolLED pE unit supplied 470nm light through a 60x objective (Olympus LUMplanFL N 60x/1.00W), measuring 83 mW/mm² maximal light intensity. Full-field stimuli were 1 ms long with power set at maximal 83 mW/mm² intensity to obtain the maximal oEPSC except in Figure S2E–F and S4C, where the duration and/or intensity of full-field stimulation were varied to describe the development of effectiveness of ChR2.

In experiments comparing multiple measurements from the same cell, such as the synaptic response to different modes of stimulation in Figures 2F and 2G and S2B, S2D–S2H, or different stimulus intensities in Figure S4C, repetitions of varying trials were interleaved. Light intensity was measured using Thorlabs Compact Power and Energy Meter (PM100D) coupled to a photodiode (S130C).

Despite embryonic onset of Cre expression (Rowan and Cepko, 2004), ChR2 expression in *Chx10-Cre;ChR2* animals is not sufficiently strong or homogeneous to drive oEPSCs in slice at immature ages (P9) (see Figure S4). Figure S4A plots the maximal NMDA oEPSC; S4B compares the maximal NMDAR eEPSC amplitudes oEPSCs from the same cell (eEPSC/oEPSC amplitude ratio) over development. We use NMDAR currents to assess ChR2 effectiveness because NMDAR maximal amplitudes are already very large at P9 (Figure S4E; Table S4, Chen and Regehr 2000), allowing comparison between the two stimulus paradigms. Moreover, unlike maximal AMPAR EPSCs, maximal NMDAR EPSCs do not change significantly between P9 and P60, allowing us to separate ChR2 efficiency from developmental changes in maximal current amplitude. At P9, full field o-stim can only recruit \sim 20% of the maximal eEPSC. The eEPSC/oEPSC ratio and the light power required to evoke maximal synaptic responses declined to mature levels between P9–16, consistent with a gradual rise in ChR2 expression (Figure S4B, S4C, Table S3).

Single Fiber Stimulation

Single RGC fiber responses were obtained using minimal electrical stimulation as previously described (Hooks and Chen, 2006; see supplemental methods, Noutel et al., 2011), or through the optic fiber positioning a spot of 470 nm light over the OT. The CoolLED control panel allows incrementing light intensity by 0.1–0.15 mW/mm² steps up to \sim 15 mW/mm², and at 0.05–0.1 mW/mm² increments up the max intensity (49 mW/mm²). We took advantage of these small increments to isolate single ChR2-expressing retinal inputs. Both 50% failure and threshold methods of SF isolation were adapted and tested for blue light stimulation. In both cases, a narrow range of light intensities around the threshold of a minimal response to stimulation was first identified manually by varying

the light intensity between ~ 0.5 – 15 mW/mm² by increments of ~ 0.1 – 0.3 mW/mm². Trials holding at -70 and $+40$ mV were alternated throughout these experiments. A window displaying a ~ 150 pA amplitude range around the baseline was used to monitor the presence of weak inputs evoked during SF isolation experiments.

For the 50% failure method, stimulation intensity was adjusted so that 50% of the trials evoked a synaptic response. For the threshold approach, which was used to obtain the majority of optical SF responses, stimulation intensity was increased every 2–4 trials until a response could be reliably evoked. As with electrical stimulation, we then gradually increased the intensity to determine whether a second SF could be isolated (a larger response exceeding the initial SF by 5x qualified as a second SF). Additional discussion of SF isolation techniques and fiber fraction can be found in supplemental procedures of [Noutel et al. \(2011\)](#) and in [Hooks and Chen \(2008\)](#).

Convergence Simulation

To calculate the number of functional RGC inputs innervating a TC neuron across development, we carried out a simulation by randomly resampling from sets of maximal and SF EPSC amplitudes. AMPAR current data were used for the P30 simulation, whereas NMDAR current data were used for P9 simulation because they are much larger and easier to measure during this age range.

SF values used for simulation: The set of 271 SFs ([Figure 4B](#)) was compiled using data from \sim P30 cells, with SF from data published in [Hong et al., 2014 \(Figure S1\)](#) and unpublished data. For the P9 simulation, an electrical stim dataset consisting of $n = 35$ SFs recorded from $n = 26$ cells in $n = 8$ P9 C57 animals were used. The proportion of silent SF inputs in these recordings (24%) was similar to that previously reported in [Chen and Regehr \(2000\)](#).

Maximal values used for simulation: All available oEPSC values from \sim P30 *Chx10-Cre;ChR2* slices were used for this dataset ($n = 68$, 1 maximal value from each cell across $n = 23$ animals). For the P9 simulation, $n = 48$ NMDAR eEPSC maximals were used (1 per cell from $n = 9$ animals). eEPSC rather than oEPSCs were used for the P9 simulation because, as shown in [Figure 4](#), 470nm light stimulation activates a much smaller proportion of RGC axons at this age than at p30. These maximal P9 eEPSCs do not incorporate inputs from severed axons and thus underestimate overall retinal drive onto P9 dLGN neurons.

The simulation: A single trial of the simulation consisted of (1) a random drawing of a maximal value, (2) random selection of SFs one by one to match the chosen maximal. Two constraints were placed on this process. (1) If the first randomly chosen SF was larger than the randomly chosen maximal, this SF was discarded and another was chosen (this was a rare occurrence). (2) SFs were randomly drawn from the source distribution until the summed amplitudes of n inputs exceeded 1.05x of the chosen maximal amplitude. The sum of n SFs and the sum of (n -(last chosen SF)) were then compared to the chosen maximal, and the set of SFs that yielded a closer value to the chosen maximal was used to tabulate the number of SFs for that simulated cell. The final set of SFs was then binned into 100-pA bins ([Figure 4E](#)).

This single trial was repeated 50,000 times for the P30 dataset and 10,000 for the P9 dataset. The resulting distribution of the number of SFs per maximal is summarized in [Figure 4](#). P9 and P30 distributions were compared using a single Mann-Whitney test on 250 randomly chosen values from each 50,000 distribution ([Figure 4G](#)). Binned SF information was used to determine the contribution of different SF amplitudes to the overall convergence. The ratio of the sum of the selected SFs and the magnitude of the chosen maximal ($\Sigma(\text{SFs})/\text{chosen maximal}$) was 0.994 ± 0.17 (Mean \pm SD) for P30 dataset and 1.034 ± 0.044 (Mean \pm SD) for the P9 dataset.

In addition to the random simulation, we considered two alternative scenarios (data not shown) in which constraints were applied to the simulation. The first was a model in which a TC neuron receives just one dominant (> 600 pA) input per simulation neuron (all other inputs must be < 600 pA). This scenario was quickly ruled out because we have multiple examples from our experiments showing that TC neurons can receive more than 1 input greater than 600 pA (data not shown). Another scenario is that at least one or more inputs onto a TC neuron must be greater than 600 pA. The results of this simulation yielded numbers similar to the initial random simulation: 9.27 ± 6.18 (mean \pm SD) inputs per simulated LGN cell, with 3.41 ± 1.84 (mean \pm SD) strong inputs. Therefore, we favor the original random simulation ([Figure 4](#)) because it lacks constraints and reflects most accurately our *in vitro* observations.

Experimental Design

Inclusion and exclusion criteria of any data or subjects: we did not exclude data.

QUANTIFICATION AND STATISTICAL ANALYSIS

Image Quantification

For quantification of cell body labeling in the visual cortex, YFP⁺ neuronal cell bodies were counted manually in ImageJ using the cell counter plugin. 4 sections each from 4 mice were used for this quantification. Across these sections, there were 14.2 ± 1.82 (Mean \pm SEM) YFP⁺ neurons per V1 L6 section; projection neurons were not distinguished from local interneurons. The number of YFP⁺ neurons was converted to a population percentage using a manually obtained density of NeuN⁺ cell bodies. This calculation showed that 0.35 ± 0.009 (Mean \pm SEM)% of NeuN⁺ cells in V1 expressed YFP; in Layer 6 of V1, $0.381\% \pm 0.016\%$ of NeuN⁺ cells were YFP⁺.

Data Analysis and Statistics

Data acquisition and analysis of voltage-clamp experiments was performed using custom software written in IgorPro (Wave-Metrics, Portland, OR), JMP (SAS Institute) and Excel (Microsoft, Redmond, WA). EPSC kinetics and paired-pulse ratios were calculated using

averages of 3-5 trials. In absence of glutamate receptors blockers for traces recorded at +40mV, the peak of the NMDAR current was measured after the initial decay of the rapid AMPAR transient.

Nonparametric tests were used throughout; two-sided p values, statistical test used, and N's for each experiment are provided in figure legends or related supplemental tables. Wilcoxon signed-rank was used for paired data, whereas Mann-Whitney and Kurskal-Wallis ANOVA with post hoc Dunn's multiple comparison test were used for unpaired data. An exception is the ANOVA used in [Figure S2D](#). All boxplots indicate the median (line within box), 25%–75% quartile range (box), and 10%–90% range (whiskers). Amplitudes are generally reported in nA unless otherwise specified. For all figures, *p < 0.05; **p < 0.01; ***p < 0.001.

Fiber Fraction Assessment

Afferent convergence was calculated by the obtaining the fiber fraction (SF current amplitude/maximal current amplitude) for each cell using electrical and light stimulation (for detailed discussion of FF, see supplemental method section of [Hooks and Chen, 2008](#)). For each cell, one eFF and/or oFF value was calculated by averaging all e-stim or o-stim AMPAR and NMDAR SF values. Electrical SF and maximal amplitude were used to calculate the eFF; SFs isolated with the optic fiber stimulus and oEPSC maximal currents were used to calculate the oFF.

Neuron, Volume 96

Supplemental Information

**Functional Convergence
at the Retinogeniculate Synapse**

Elizabeth Y. Litvina and Chinfei Chen

Supplemental Figures and Tables:

Chx10-Cre; ChR2-eYFP^{f/wt}

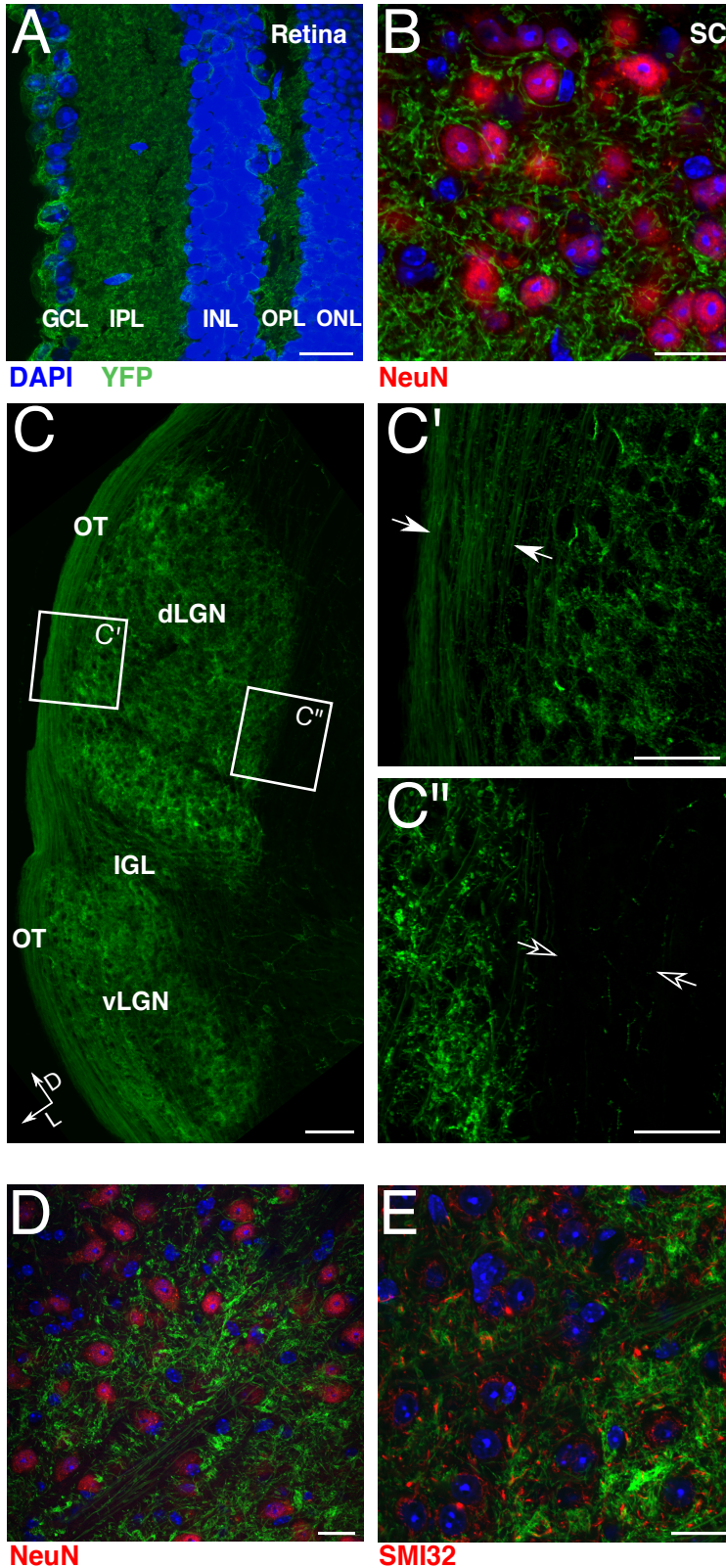


Figure S1: ChR2 expression is restricted to retinogeniculate afferents in *Chx10-Cre;ChR2* mice. Related to Figure 1.

(A) Transverse section (confocal z-stack) of a *Chx10-Cre;ChR2* retina shows expression of YFP in multiple layers of the retina, including RGC layer. (B) High-magnification view of the superior colliculus (SC) showing YFP⁺ axons and bouton clusters (green), NeuN-positive cell bodies (red), and DAPI-stained nuclei (blue); YFP expression is strictly absent from SC somas. (C)

Representative tiled confocal image of geniculate YFP labeling in *Chx10-Cre;ChR2* mouse. Inset views of YFP labeling in Optic Tract (OT) and its absence in the Corticothalamic Tract (CT) indicated in boxes. C', C'':

Magnified views of corresponding boxed regions in C; filled arrows indicate YFP⁺ retinal axons in the OT, and empty arrows indicate near-complete absence of YFP signal in the region where corticothalamic axons enter the dLGN. IGL: Intergeniculate leaflet; vLGN: ventral LGN. dLGN: dorsal LGN. (D-E) High-magnification view of the dLGN showing ChR2 expression in retinal axons (green) with (D) NeuN staining for neuronal cell body (red), and DAPI-stained nuclei (blue), or (E) SMI32⁺ proximal TC neuron dendrites (red), and DAPI-stained nuclei (blue). YFP expression is exclusively in the neuropil and not present in the soma or dendrites of dLGN neurons. Scale Bar A, B, D, E=20μm, C=100 μm, C', C''=50 μm.

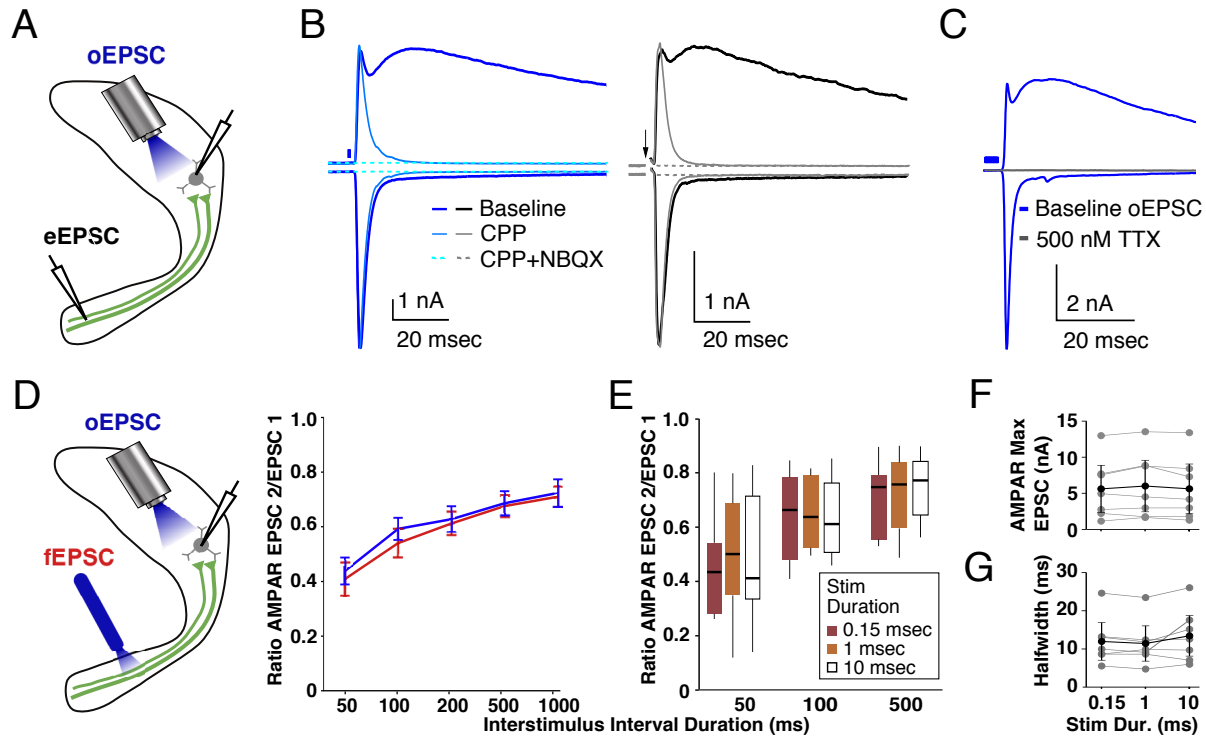


Figure S2: No Evidence of Disrupted Neurotransmitter Release with Full-Field ChR2 Stimulation. Related to Figure 2.

(A) Experimental schematic for Figure S2B. (B) oEPSCs and eEPSCs have similar kinetics and pharmacologic sensitivity. (*Left*), oEPSCs (blue traces) and (*Right*), eEPSCs (gray, and black traces) recorded at -70 and +40 mV before (darkest shade) and following the addition of CPP (20 μ M, thin light blue and gray lines) and NBQX (5 μ M, dashed lines) from the same P32 TC neuron. Traces average 3-5 trials. (C) Application of 0.5 μ M TTX completely abolishes the oEPSC. Similar results were obtained from n=6 slices, mice aged P55-100; traces are average of 3 trials. (D) (*Left*) Experimental Schematic. (*Right*) Comparison of the response to pairs of pulses from ChR2 expressing RGC axons evoked by action potential mediated depolarization of presynaptic boutons (fEPSC, red) and direct depolarization of presynaptic boutons (oEPSC, blue). Both modes of stimulation result in similar paired pulse responses. Error bars: SEM. (E-G) Paired-pulse depression (E; P=0.9 Two-way ANOVA; Box: 25-75% IQR; whiskers 10-90% IQR), AMPAR EPSC amplitude (F; p>.09 Wilcoxon; error bars: SEM), and halfwidth of AMPAR oEPSCs (G; P>0.15 Wilcoxon; error bars: SEM.) do not vary with blue light stimulation duration (0.15, 1, and 10 msec). Grey connected data points in F,G compare measurements from the same cell.

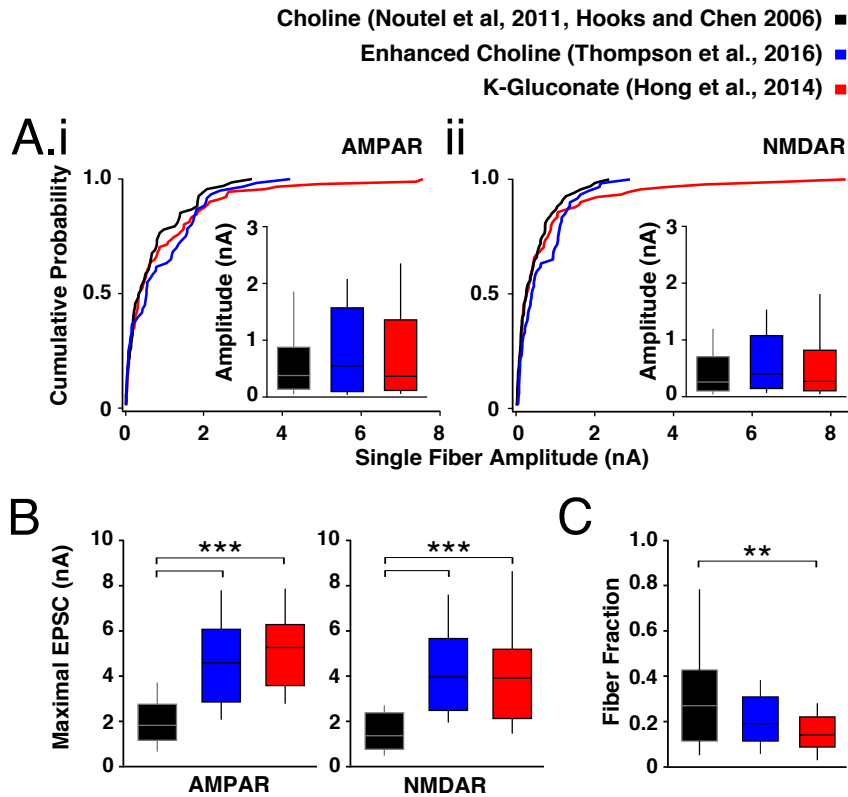


Figure S3: Higher convergence identified in healthier retinogeniculate slices. Related to Figure 3.

A comparison of published data from mouse retinogeniculate slices prepared in three different cutting solutions (see methods). Enhanced Choline and K-gluconate cutting solutions improve the health of the slice relative to standard choline. (A) Cumulative probability distributions of AMPAR (i) and NMDAR (ii) SF amplitudes from the three cutting solutions are similar. Insets: box plot representation of the same data. N.S. K-W with Dunn. (B) Maximal AMPAR (*Left*) and NMDAR (*Right*) EPSC amplitudes are larger in healthier slices. *** $p < 0.0001$ K-W with Dunn. (C). Healthier slices yielded a lower fiber fraction estimate of convergence. ** $p < 0.001$ K-W with Dunn. For all panels, box: 25-75% IQR; whiskers 10-90% IQR.

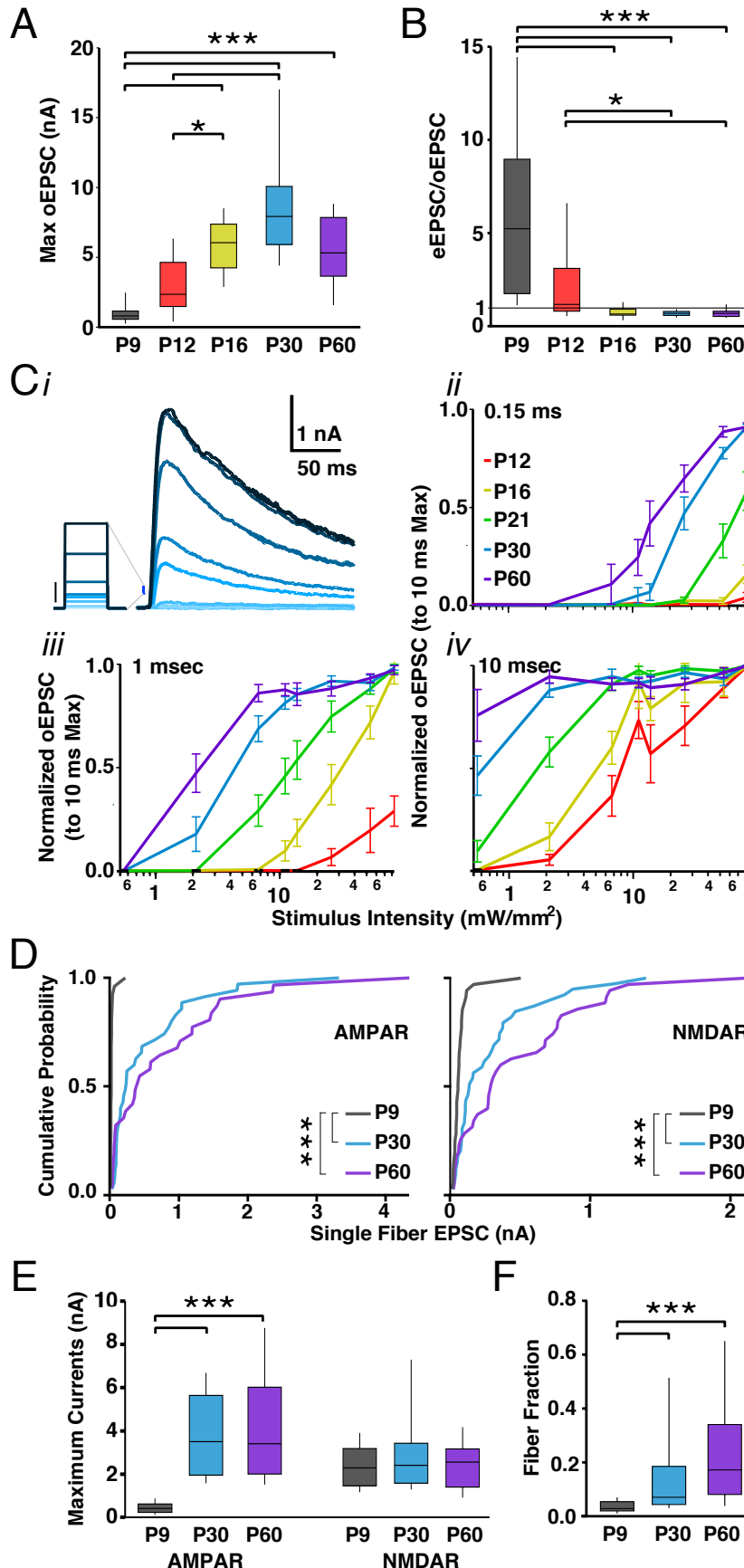


Figure S4: Developmental Assessment of Convergence with Optogenetics is Limited by Chr2 expression. Related to Figure 4.

To assess effectiveness of optogenetic stimulation in *Chx10-Cre;Chr2* mice over development, we examined maximal NMDAR currents as they are already very large at P9 and therefore allow ease of comparison between the oEPSC and eEPSC. (A) The amplitude of NMDAR oEPSCs increases from P9-P16. However, this increase does not reflect a developmental change in synaptic strength, as maximal NMDAR eEPSCs do not significantly increase in amplitude between P9 and P60 (see panel E). (B) The ratio of maximal NMDAR eEPSCs to oEPSCs (using full power 10 msec light pulses) over age provides a measurement of the proportion of electrically vs optically-accessible retinogeniculate axons. eEPSCs are much larger than oEPSCs at P9 and P12, but oEPSCs exceed eEPSCs after P16. Thus, Chr2 expression in the RGC population does not become fully effective until p16. (C) The light power needed to evoke maximal oEPSC responses decrease over age, consistent with a gradual rise in Chr2 expression. (i). Example (P21) recording of oEPSCs evoked with 470 nm light (1 msec) of increasing intensities; traces are the average of 3-5 trials. Color scale of light intensity is

indicated in the stimulus steps on the left. The vertical scale bar represents 20 mW/mm². (*ii-iv*) The NMDAR oEPSC amplitude, normalized within each cell to the maximal response evoked with full power 10 msec long light pulse, is plotted against the stimulus intensity for different durations of blue light pulses (0.15 (*ii*), 1 (*iii*), and 10 (*iv*) msec). Consistent with low ChR2 expression during development, much higher and longer light intensities are required to activate the maximal response in younger than older animal. As shown in B, these maximal responses in younger animals are smaller than the maximal response to electrical stimulation. Error bars: SEM. (D-F) Reexamining FF over development from healthier slices using e-stim from P9, P30, and P60 mice. (D) Both the SF AMPAR and NMDAR EPSCs are much smaller before eye opening than at P30 or P60. (E) Maximal AMPAR eEPSCs dramatically increase over development, whereas maximal NMDAR eEPSCs are robust before eye opening. (F) eFF significantly increases after eye opening. The P30 data in Figs D-F replots eEPSC data presented in Figure 3 and Table S2. Detailed statistics in Tables S3, S4. *p<0.05; ***p<0.001. Panels A, B, E, F: Box 25-75% IQR; whiskers 10-90% IQR)

Table S1: Data Table Related to Figures 2E, F-G.

(Top) Analysis of AMPAR and NMDAR EPSC maximals obtained with electrical and full-field optical stimulation of retinal inputs to the dLGN. (Bottom) Comparison of AMPAR EPSC amplitude and kinetics in response to three types of stimulation (full-field, electrical, and optic fiber) recorded from the same cells. Q=quantile

Matched Maximal EPSCs							
N Mice	13						
N Cells	24						
	AMPA (nA)		NMDA (nA)		AMPA:NMDA Ratio		oEPSC:eEPSC (AMPA and NMDA)
Stim Type	oEPSC	eEPSC	oEPSC	eEPSC	oEPSC	eEPSC	
Median	4.93	3.23	4.09	1.93	1.38	1.38	1.71
75% Q	8.63	5.33	7.21	3.91	2.04	1.73	2.52
25% Q	3.43	2.08	2.67	1.40	0.92	1.00	1.27
Mean	6.45	3.75	5.53	3.08	1.48	1.41	2.13
SEM	0.83	0.43	0.92	0.52	0.13	0.12	0.32
Wilcoxon (paired) p value	<0.0001		<0.0001		<0.66		

Matched Maximal EPSCs						
N Mice	13					
N Cells	24					
	EPSC Peak (nA)			Normalized Halfwidth (ms/nA)		
Stim Type	eEPSC	fEPSC	oEPSC	eEPSC	fEPSC	oEPSC
Median	6.01	5.46	10.71	1.55	1.81	1.59
75% Q	8.64	6.99	13.14	2.55	2.69	2.31
25% Q	4.50	3.31	7.53	1.34	1.45	1.08
Mean	6.84	5.65	10.36	2.24	2.97	2.05
SEM	0.84	0.75	0.97	0.60	0.87	1.79
Wilcoxon (paired) p value	eEPSC	0.0574	<0.001		0.08	0.79
	fEPSC		<0.001			0.08

Table S2: Detailed single fiber, maximal, and fiber fraction data for Figure 3C-E.

Table summary of Figure 3C-E, showing optically and electrically evoked data from the same set of cells. This set of Maximal EPSCs is distinct from the set shown in Figure 2/Table S1.

N=12 mice	Single Fiber EPSC (nA)				Maximal EPSC (nA)				Fiber Fraction		eFF:oFF
	AMPA		NMDA		AMPA		NMDA		eFF	oFF	
	eEPSC	fEPSC	eEPSC	fEPSC	eEPSC	fEPSC	eEPSC	fEPSC			
N SF or Cell	23				16				16		16
Median	0.24	0.27	0.23	.15	3.34	5.88	2.37	4.84	0.12	0.06	1.57
75% Q	0.95	0.81	0.09	0.07	5.48	8.61	1.43	3.49	0.20	0.09	3.59
25% Q	0.10	0.11	0.61	0.66	1.87	4.09	3.08	5.69	0.06	0.33	1.06
Mean	0.64	0.65	0.37	0.42	3.58	6.52	2.47	5.48	0.21	0.12	3.81
SEM	0.17	.018	0.08	0.12	0.47	0.88	0.31	0.81	0.06	0.05	1.55
Wilcoxon (paired) p value	0.99		0.79		0.0021		<0.0001		0.01		

Table S3: Detailed analysis and statistical test for assessment of the development of Chr2 expression shown in Figure S4A-C. IQR=Interquantile Range (25-75%)

Peak NMDAR oEPSC Amplitude (nA)										
Age	P9	P12	P16	P30	P60	KW with Dunn p values				
N Animals	5	6	4	4	4		P9	P12	P15	P30
N cells	13	23	13	18	15	P9				
Median	0.81	2.35	6.05	7.92	5.32	P12	0.4956			
IQR	0.58	3.15	3.13	4.15	4.21	P16	0.0002	0.049		
Mean	0.99	2.95	5.89	8.67	5.45	P30	<0.001	<0.001	1	
SEM	0.20	0.46	0.52	0.92	0.67	P60	0.0006	0.1091	1	0.61
NMDAR eEPSC/oEPSC										
Median	5.23	P12	0.65	0.68	0.68	P12	0.3074			
IQR	7.21	P16	0.32	0.21	0.28	P16	0.0004	0.1316		
Mean	5.88	P30	0.76	0.68	0.71	P30	<0.0001	0.0088	1	
SEM	1.29	P60	0.08	0.04	0.07	P60	<0.0001	0.0122	1	1
Peak NMDAR eEPSC Amplitude (nA)										
Median	3.31	P12	3.88	5.07	3.28	P12	1			
IQR	3.50	P16	2.32	2.95	2.32	P16	1	1		
Mean	3.92	P30	4.36	5.62	3.65	P30	0.4105	0.00153	1	
SEM	0.64	P60	0.60	0.50	0.46	P60	1	1	1	0.17

Table S4: Detailed single fiber, maximal, and fiber fraction change over development, related to Figure S4D-F.

		Single Fiber EPSC (nA)					
		AMPA			NMDA		
Age Group		P9	P30	P60	P9	P30	P60
N Mice		8	13	10	8	13	10
N SF or Cell		26	31	31	35	31	31
Median		0.02	0.23	0.40	0.06	0.17	0.28
75% Q		0.02	0.89	0.12	0.08	0.38	0.68
25% Q		0.01	0.10	0.07	0.04	0.09	0.06
Mean		0.02	0.56	0.78	0.07	0.31	0.44
SEM		0.01	0.13	0.17	0.01	0.17	0.08
KW/Dunn p value >	P30	0.0001			0.0001		
	P60	0.0001	1		0.0001	1	
		Maximal EPSC (nA)					
		AMPA			NMDA		
Age Group		P9	P30	P60	P9	P30	P60
N Mice		8	13	10	9	17	11
N SF or Cell		28	23	18	28	23	18
Median		0.28	3.50	3.41	2.29	2.41	2.56
75% Q		0.27	5.64	6.03	3.19	3.43	3.17
25% Q		0.60	1.95	2.00	1.46	1.58	1.40
Mean		0.45	3.87	4.18	2.39	2.98	2.44
SEM		0.04	0.37	0.41	0.30	0.33	0.38
KW/Dunn p value >	P30	0.0001			1		
	P60	0.0001	1		1	1	
		Fiber Fraction			AMPA:NMDA Ratio		
Age Group		P9	P30	P60	P9	P30	P60
N Mice		8	13	10	9	17	11
N SF or Cell		28	23	18	49	43	28
Median		0.03	0.07	0.17	0.19	1.34	1.57
75% Q		0.05	0.19	0.34	0.13	1.01	1.23
25% Q		0.02	0.04	0.08	.025	1.77	2.03
Mean		0.05	0.17	0.23	0.20	1.45	1.64
SEM		0.01	0.05	0.05	0.01	0.08	0.11
KW/Dunn p value >	P30	0.0001			0.0001		
	P60	0.0001	0.60		0.0001	1	